



Correlated disorder by defects clusters in LiNbO₃ single crystals after crystal ion-slicing

Simone Dolabella^{a,b}, Alexandre Reinhardt^c, Ausrine Bartasyste^d, Samuel Margueron^d, Amit Sharma^e, Xavier Maeder^e, Alex Dommann^a, Antonia Neels^{a,b}, Aurelio Borzi^{a,*}

^a Center for X-ray Analytics, Swiss Federal Laboratories for Materials Science and Technology, Empa, Überlandstrasse 129, 8600 Dübendorf, Switzerland

^b Department of Chemistry, University of Fribourg, Chemin du Musée 9, 1700 Fribourg, Switzerland

^c Univ. Grenoble Alpes, CEA, Leti, 38000 Grenoble, France

^d FEMTO-ST Institute, Université Bourgogne Franche-Comté, CNRS UMR 6174, ENSMM, 26 rue de l'Épitaphe, Besançon, France

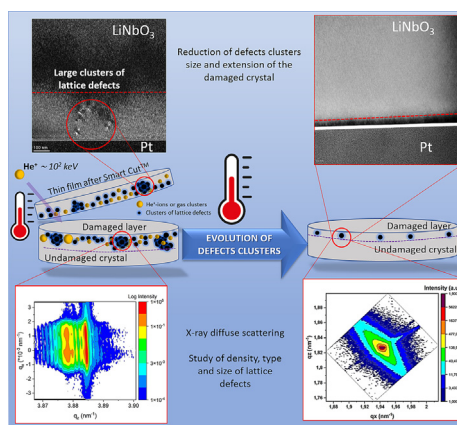
^e Mechanics of Materials and Nanostructures, Swiss Federal Laboratories for Materials Science and Technology, Empa, Feuerwerkerstrasse 39, 3602 Thun, Switzerland

HIGHLIGHTS

- Optimal recovery of crystal ion slicing-processed LiNbO₃ crystallinity achieved through 2 h, 200 °C annealing post crystal-ion-slicing.
- The recovery of the crystallinity involves the rearrangement of CIS-induced point defects and their clusters into dislocation loops and cascade.
- Post-CIS annealing at temperature 200 °C above the split temperature induces non-correlated dislocations and increases the in-plane stress.
- The findings in this work support the optimization of the design of LiNbO₃ thin-film bulk acoustic wave filters.

GRAPHICAL ABSTRACT

Reducing the irradiation damage in materials processed by crystal ion slicing (CIS) is pivotal for recovering the properties linked to the materials' structure, which enables the performance of related devices. The study of the X-ray diffuse scattering allows to understand the mechanism of thermal recrystallization in CIS-processed materials, which facilitates the optimal design of the crystallinity recovery process.



ARTICLE INFO

Article history:

Received 13 January 2023

Revised 9 May 2023

Accepted 11 May 2023

Available online 15 May 2023

Keywords:

LiNbO₃

Crystal ion-slicing

High-resolution X-ray diffraction

Diffuse X-ray scattering

ABSTRACT

LiNbO₃ (LNO) is a material suitable for high-frequency and wideband RF filters as well as photonic applications due to its outstanding piezoelectric and optical properties. Applications such as thin-film bulk acoustic wave resonators or highly confined electro-optic modulators require thin films, which are still challenging to be obtained with the necessary crystalline quality by deposition methods. Alternatively to deposition, crystal ion-slicing (CIS) or Smart Cut™ enables obtaining thin films hundreds of nanometers thick from the bulk single-crystal utilizing high-energy and dose implantation of light atoms. The price to pay is the partial degradation of the initial crystalline perfection, which translates to a degradation of the piezoelectric performance of the material if the CIS-induced damage is not eliminated.

This work aims to understand the physics of the recrystallization process of the CIS-damaged LNO crystal upon thermal annealing. The study of the coherent and diffuse scattering by high-resolution X-ray

* Corresponding author at: Center for X-ray Analytics, Empa, Überlandstrasse 129, CH-8600 Dübendorf, Switzerland.

E-mail address: aurelio.borzi@empa.ch (A. Borzi).

diffraction, complemented by micro-Raman backscattering spectroscopy and Transmission Electron Microscopy (TEM), allowed to study the recovery of the crystallinity from the CIS-induced lattice strain and stress and the progressive reduction of the defects clusters dimension.

© 2023 The Author(s). Published by Elsevier Ltd. This is an open access article under the CC BY license (<http://creativecommons.org/licenses/by/4.0/>).

1. Introduction

LiNbO₃ (LNO) and LiTaO₃ (LTO) are among the most promising materials for integrated optics and RF devices because of their electro-optical, nonlinear optical, and piezoelectric properties. Using these materials as optical waveguides requires the formation of layered structures, which can be achieved by high-temperature ion diffusion or implantation of high-energy light elements, such as H⁺ or, more often He⁺ [1–5]. As for piezo acoustic applications, trends such as temperature stability, operation at high frequencies (up to 6 GHz), and broad bandwidth push Surface Acoustic Wave (SAW) or Bulk Acoustic Wave (BAW) currently in use to their limits, primarily due to the limited electromechanical factors of the waves exploited [6]. In the field of Bulk Acoustic Wave (BAW) filters, alloying Aluminum Nitride (AlN) shows promising results, even though the electromechanical coupling factors will probably keep limited to 20% [6]. In this frame, LiNbO₃ and LiTaO₃ are receiving considerable interest because of their outstanding electromechanical coupling factors, and researchers are going on to integrate the material into filters of different designs [7,8]. These works have revealed the potential for extremely large electromechanical coupling resonators, up to 40 % [6].

The use of LiNbO₃ for the fabrication of BAW filters operating at high frequency (in the GHz range) requires these materials in the form of thin films with thicknesses below one micrometer. However, depositing a thin film of such a crystal with the required crystalline quality is challenging [9]. A method to obtain thin films from the CZ bulk single-crystal is based on the implantation of light atoms such as H or He at high energy and dose, followed by thermal processes that enable the splitting of a thin film of the implanted materials [6,10]. The technique, called crystal ion slicing (CIS) or Smart Cut™, has been successfully used in the fabrication of thin-film bulk acoustic wave resonators (TFBAR) [6]. Both for optical and piezo-acoustic applications, the aspiration is to maintain the crystalline structure of the materials as much as possible unaffected by the ion-slicing, since the optical and piezoelectric properties are manifestations of the crystalline structure itself. On the other hand, the implantation and subsequent thin-film splitting damage the crystalline structure, introducing point defects such as vacancies, interstitials and substitutional, defects clusters, and amorphization [11–13]. Fig. 1 shows the effect of implanting an X-cut LiNbO₃ single crystal with He-ions at doses and energy usually involved in the CIS process. The LNO 110 reflection appears broadened in both directions of the reciprocal space. The profile along q_z in Fig. 1(b) shows the extended structure and the Laue fringes, which stands for the formation of a well-defined interface at the ions stopping range. At each q_z diffraction maxima, the diffracted intensity are spread out along the q_x direction due to the presence of lattice defects introduced during ion implantation. The distance between the fringes points out that the stopping range is located at around 735 nm from the surface, enabling the split and transfer of a sub-micron LiNbO₃ thin film for FBAR applications.

High-temperature annealing of implanted crystals enables partial recovery from the CIS-induced crystalline damage, consequently improving the related physical properties. The effect of the thermal annealing on implanted LiNbO₃ single crystals was investigated by Zolotoyabko [14] and Avrahami [15], who described

the progressive reduction of the extended structure when increasing the annealing temperature. Avrahami and coworkers defined a critical temperature $T_c = 200$ °C above which the implanted crystal undergoes a defects-clustering phenomenon, which brings the optical waveguide barrier to be destroyed or the lift-off of the part of the crystal above the stopping range in the case of ion-slicing applications [15]. Many annealing protocols have been developed to answer the specific demands of specific fabrication processes [10,11,16–19]. In any case, the annealing parameters, such as the temperature, atmosphere, time, and the possible use of etching agents, strictly depend on the implantation / CIS conditions and the final application of the crystal. For this reason, the identification of a thermal treatment protocol is not the object of this paper. Instead, this study aims to understand the influence of thermal annealing on the evolution of the CIS-induced lattice defects in LNO single-crystal, investigating the structural transformations involved in the recrystallization process.

For applications related to the crystal ion slicing, the CIS-processed material can be considered as the starting point. The materials undergo extensive processing during the CIS, which involves itself a high-temperature step to promote the coalescence of the gas clusters in more giant platelets until the thin film splitting, which differentiates deeply the post-CIS microstructural status from the post-implantation one. The split temperature depends on the ion implantation parameters, i.e. dose and energy; however, the physical phenomena bringing to the splitting are supposed to remain unvaried, as well as the status of the crystallinity after the layer split. For this reason, it appears more reasonable that physical phenomena related to the recrystallization are described in a scale of temperature relative to the split temperature. Reporting the absolute temperatures might be less informative because of the dependence of the split temperature on the implantation parameters, often hidden for the sake of confidentiality when industrial processes are involved.

In this work, we started from the as-split (or post-CIS) LNO crystal and performed thermal annealing at temperatures up to 300 °C above the splitting one. The maximum annealing temperature represents a threshold, above which the LiNbO₃ congruent crystal undergoes compositional changes due to Li, O, and Li₂O evaporation [20]. The influence of thermal annealing on the structure of post-CIS X-cut black LiNbO₃ single crystals has been evaluated by high-resolution X-ray diffraction (HRXRD), complemented by Raman backscattering spectroscopy and transmission electron microscopy (TEM). The initially implanted LNO wafer was used instead of the split thin film; on the one hand, this avoids the influence of other materials deposited during the fabrication process and before the CIS on the HRXRD analyses. On the other hand, the implanted wafer after the CIS still contains crystalline damage, which was proved by X-ray diffraction and measurements of the piezoacoustic performance.

X-ray diffraction (XRD) is among the most established methods for microstructural investigations and the study of order–disorder transitions, chemical composition, crystalline phases, preferred orientation and texture, [21] size of crystallites [22–24], microstrain, and defects densities and mobility [24–27]. The extensive processing and utilization of bulk single crystals and high-quality epitaxial thin films by the microelectronic industry required the improvement of the analytical performances of XRD instruments, opening the floor to high-resolution X-ray diffraction (HRXRD)

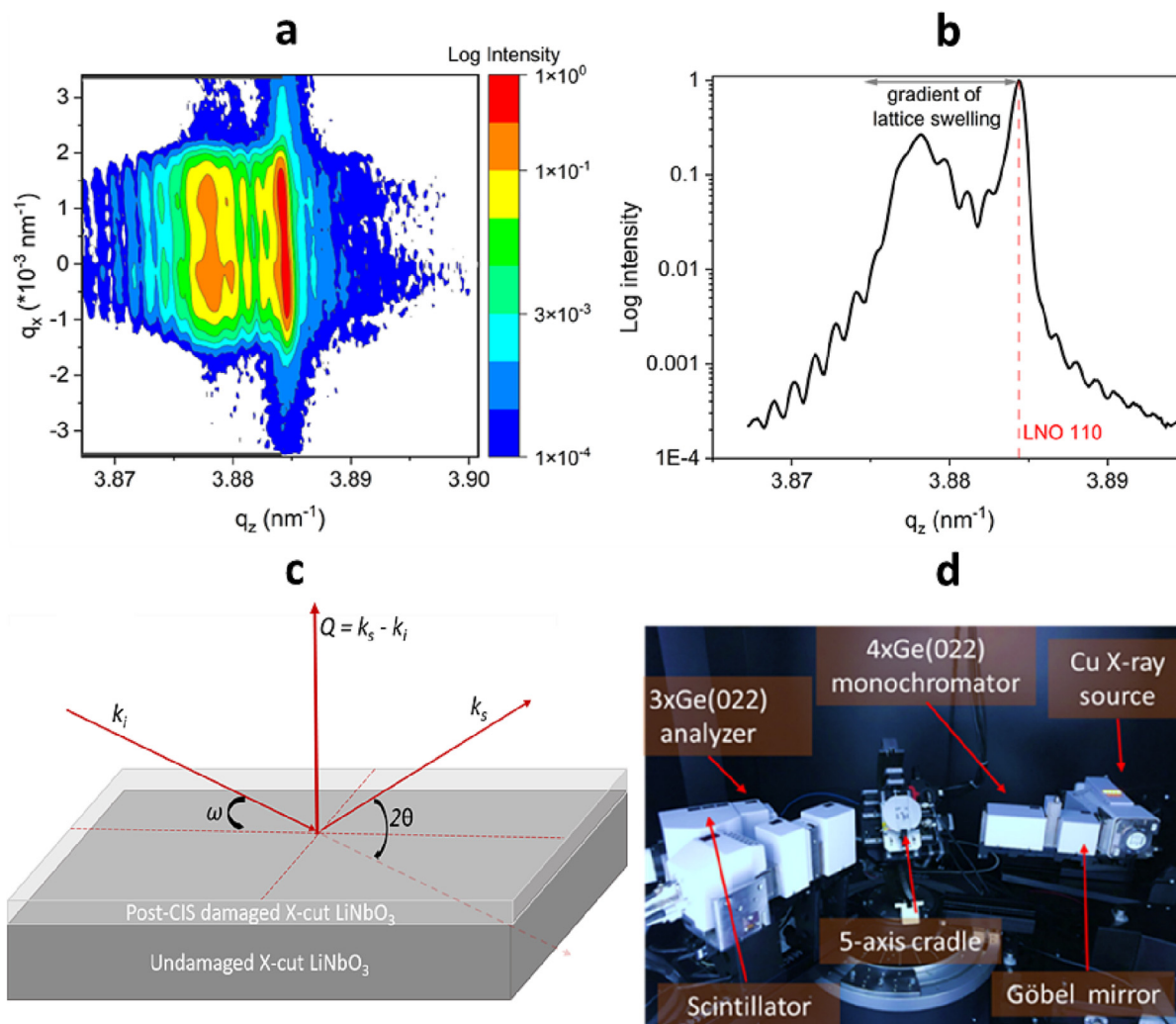


Fig. 1. (a) Reciprocal space map around the LNO 110 lattice point after He⁺-implantation. The high dose produces severe crystalline damage both in the direction radial (swelling gradient of the d_{110} -spacing) and azimuthal around the LNO(110); (b) q_z profile at $q_x = 0 \text{ nm}^{-1}$ extracted from the RSM in (a). The gradient of the lattice swelling is visible as an extension of the scattered intensities at smaller values of momentum transfer along q_z than the theoretical for the LNO 110 (marked with a red dashed line). The Laue fringes mark the formation of a well-defined interface at the He-ions stopping range, corresponding to a depth equal to 735 nm; (c) HRXRD experimental configuration with the most important exploited angles. (d) Bruker D8 Discover DaVinci is equipped with high-resolution optics of the primary beam (Göbel mirror and Bartels monochromator) and diffracted beam (3xGe(220) crystal analyzer). (For interpretation of the references to color in this figure legend, the reader is referred to the web version of this article.)

[26,28–33]. HRXRD is a powerful method for exploring the microstructure or highly ordered systems because of its unrivaled high lattice strain sensitivity [34].

The analysis of the X-rays scattered in the region of the Bragg's peak provides different information as a function of the type of scan - radial $\theta/2\theta$ scans, angular scans or rocking curves (RC), reciprocal space maps (RSMs). The diffuse X-ray scattering, i.e., the radiation scattered in regions of the reciprocal space relatively far from the lattice point node, provides insightful structural information [35].

The vibrational states of crystals are strongly dependent on atomic distances, strength of atomic bonds, which can be modified by the presence of the crystalline defect. These defects are normally revealed by changes in the Raman shift value or in the width of the bands. In particular, degradations of the LiNbO₃ microstructure were found to decrease the intensity of peaks and broaden the linewidths of the Raman modes [36]. In this study, micro-Raman backscattering spectroscopy has been employed to evaluate the effect of thermal annealing on the material structure.

Our study discusses phenomena experimentally and provides explanations based on coherent and diffuse scattering theories, complemented by Raman spectroscopy and TEM images.

2. Materials and methods

The sample under study is a 525 μm -thick LiNbO₃ (LNO) single crystal wafer cut along the (110) crystallographic direction (X-cut). The present LNO crystal belongs to the centrosymmetric trigonal system with space group R-3c and lattice parameters $a = b = 5.149 \text{ \AA}$ and $c = 13.862 \text{ \AA}$ [37]. Additional information about the samples fabrication process can be found in work from Moulet and coworkers [38]. After the CIS and the surface polishing, the implanted wafer still presents residual CIS-induced crystalline damage, analogue to that in the sliced thin film. The wafer was diced into pieces $2 \times 2 \text{ cm}^2$: four parts were annealed in air, for 2 h, in a range of temperatures from + 100 °C to + 300 °C with respect the split temperature.

High-resolution X-ray diffraction (HRXRD) measurements were performed using a BRUKER D8 DaVinci instrument equipped with high-resolution optics for the primary and scattered beam, as shown in Fig. 1(b). The X-ray beam is generated by a Cu-sealed source and collimated by a Göbel mirror. A Bartels four-crystal symmetrical Ge(220) channel-cut monochromator is mounted to limit the energy and angular divergence of the primary beam. A

triple-crystal symmetrical Ge(220) channel-cut crystal analyzer is mounted in front of the scintillation detector to reduce the angular and energetic acceptance to the detector. Materials microstructure was investigated by performing Reciprocal Space Maps (RSMs), i.e., $(\omega + \omega_0) - 2\theta$ scans at different ω_0 offsets. The width of the line beam in the scattering plane was selected using a 600 μm slit and kept constant for all the measurements. The length of the beam in the direction perpendicular to the scattering plane is not reduced so that samples are illuminated over the entire length. The HRXRD experimental configuration concerning the investigated angles of interest is shown schematically in Fig. 1(c), and the corresponding diffractometer instrument in Fig. 1(d). Instead of angular units, reciprocal space units are used, which is particularly convenient for evaluating diffuse scattering. In particular, the scattering vector modules are expressed in \bar{q}_z and \bar{q}_x , where $\bar{q}_z = \bar{Q}_z/2\pi$, and $\bar{Q}_z = 4\pi \cdot \sin(\theta) \cdot \lambda^{-1}$ related to the geometry exploited in this work. \bar{Q}_x is here always expressed in relative scale. The main focus of the work is on the diffuse scattering analysis, which does not require an extremely high angular resolution, the angular steps of the radial and angular axis were set to 0.01° , equivalent to 0.0011 nm^{-1} in q when Cu radiation is exploited. Accordingly, the accuracy related to the exploited experimental configuration is estimated to be $\pm 0.001 \text{ nm}^{-1}$.

Micro-Raman backscattering spectroscopy measurements have been performed by using S&I MonoVista Raman spectrometer with a Nd:YAG 532 nm laser, finely focused onto the sample surface through a 100X microscope objective. The spatial lateral resolution and depth penetration of the laser into LiNbO₃ are around 1 μm . To evaluate the crystallinity of LNO, we collected Raman spectra in the X(YZ) \bar{X} backscattering geometry. Backscattering arrangements are in the standard Porto notation. The first letter (X) refers to the propagation direction of the incident photons, normal to the surface of the X-Cut LiNbO₃ wafer. The letters inside the brackets (YZ) refer to the polarization direction of the incident and scattered photons, respectively. These are controlled by polarizers positioned along with the incident and scattered wave path. The last letter (\bar{X}), refers to the propagation direction of the scattered light, so the same (with opposite verse) with respect to the incident one in Raman backscattering analysis. Raman modes were identified according to the assignment given in ref. [39]. The spectra were calibrated by recording the spectra of a X-LiNbO₃ single crystal with a congruent composition (48.34 mol. % of Li₂O) for an equivalent polarization configuration. Given the high sensitivity of Raman spectroscopy data to the temperature, all measurements were collected at the same environmental conditions. The residual stresses were calculated from the shifts of wavenumbers of E(1TO) and E(6TO) modes with respect to their wavenumbers in unstressed bulk LiNbO₃ as detailed in ref. [40].

TEM lamellae from pristine and annealed samples were prepared using a FIB (Tescan Lyra FEG). The bright field (BF) and weak beam dark field (WBDF) were acquired using a ThermoFischer Themis 200 G3 Transmission Electron Microscope (TEM) operating at 200 kV and corrected for spherical aberration. A double tilt sample holder was used to obtain the two-beam condition for weak beam dark field imaging.

3. Results

3.1. Coherent scattering

Conventional X-ray coherent scattering measurements have been performed through HRXRD. In this work, information on the coherent scattering, in the near-Bragg region, are mainly obtained by measurements around the (110) out-of-plane

direction; this is because of the highest angular resolution achievable by the symmetrical coplanar geometry. Fig. 2 shows the RSMs collected in the vicinity of the (110) (a-d) and (012) (e-h) LiNbO₃ lattice points, respectively. This corresponds to the broadening of the Bragg's peaks in the reciprocal space along the directions (110) out-of-plane and the (012), with which it forms an angle of 43.25° . Measurements along the (012) were performed in symmetrical non-coplanar diffraction geometry, which is associated to partial angular resolution loss. For this reason, the 012 reflections are used to perform the study on the diffuse X-ray scattering, which is not affected by the partial loss in angular resolution.

Fig. 3(a) reports the 1D profiles along q_z and q_x extracted from the RSMs, while positions and broadening of the profiles are plotted in Fig. 3(b-d). After the crystal ion-slicing, two maxima appear in the RSM along q_z . The maxima are separated in reciprocal space, with $\Delta q_z = 0.0062 \text{ nm}^{-1}$. The node at the larger scattering vector module comes from the undamaged crystal substrate, while the second maximum at smaller scattering vector module is the result of the residually damaged crystal after the ion-slicing. The presence of a double peak along the (110) radial direction, clearly visible from the black profile in Fig. 3(a), is a consequence of the lattice swelling, caused by the ion implantation and CIS in the damaged part of the crystal. The distribution of the scattered intensities along q_z is broader by one order of magnitude for the component related to the damaged part of the crystal compared to the undamaged substrate. The thermal annealing at 100 °C above the split temperature is sufficient to promote the recrystallization of the damaged part of the crystal. This translates into the disappearance of the diffraction node and peak at a smaller scattering vector module, as shown in Fig. 2(b) and the extracted blue profile in Fig. 3(a). Further increasing the annealing temperature does not cause any major change in the distribution of the coherent Bragg scattering along q_z .

Observing the distribution of the coherent Bragg scattering along the azimuthal direction, i.e., q_x , it extends over the same range for both the undamaged substrate and damaged residual layer in the post-CIS crystal, as shown in the inset in Fig. 3(a). The spread of the scattered intensities along q_x remains substantially unvaried after annealing above the splitting temperature as far as the exploited experimental resolution allows to determine. However, the annealing at the maximum temperature, 300 °C above the splitting, causes a significant broadening of the coherent scattering distribution along q_x , which spreads out of a range equal to $0.0021(2) \text{ nm}^{-1}$.

3.2. Diffuse scattering

Diffuse X-ray scattering (DXS) analyses have been performed around the (012) of LiNbO₃. The presence of scattered intensity relatively far from the Bragg lattice point is clear when observing the RSMs in Fig. 2. The variation in the DXS behavior with the annealing temperature along both crystallographic directions (110) and (012) is noteworthy. In particular, the diffuse scattering upon annealing at 100 °C and 200 °C appears much broader around the (012) compared to the (110), in both the azimuthal and radial directions. Upon annealing at 300 °C above the split temperature we observe an opposite behavior of the DXS distribution, which points out rearrangements of the crystalline disorder associated to the generation of diffuse scattering into crystalline disorder impacting the coherent scattering. Fig. 4 shows the logarithmic intensity distribution profiles along q_z relative, q_x relative, and $\text{Log}(q_x \text{ relative})$.

The profiles along q_z and q_x appear broadened in the region of the tails with respect to a Gaussian behavior. Along q_z , the most insightful information relates to the presence of asymmetries that

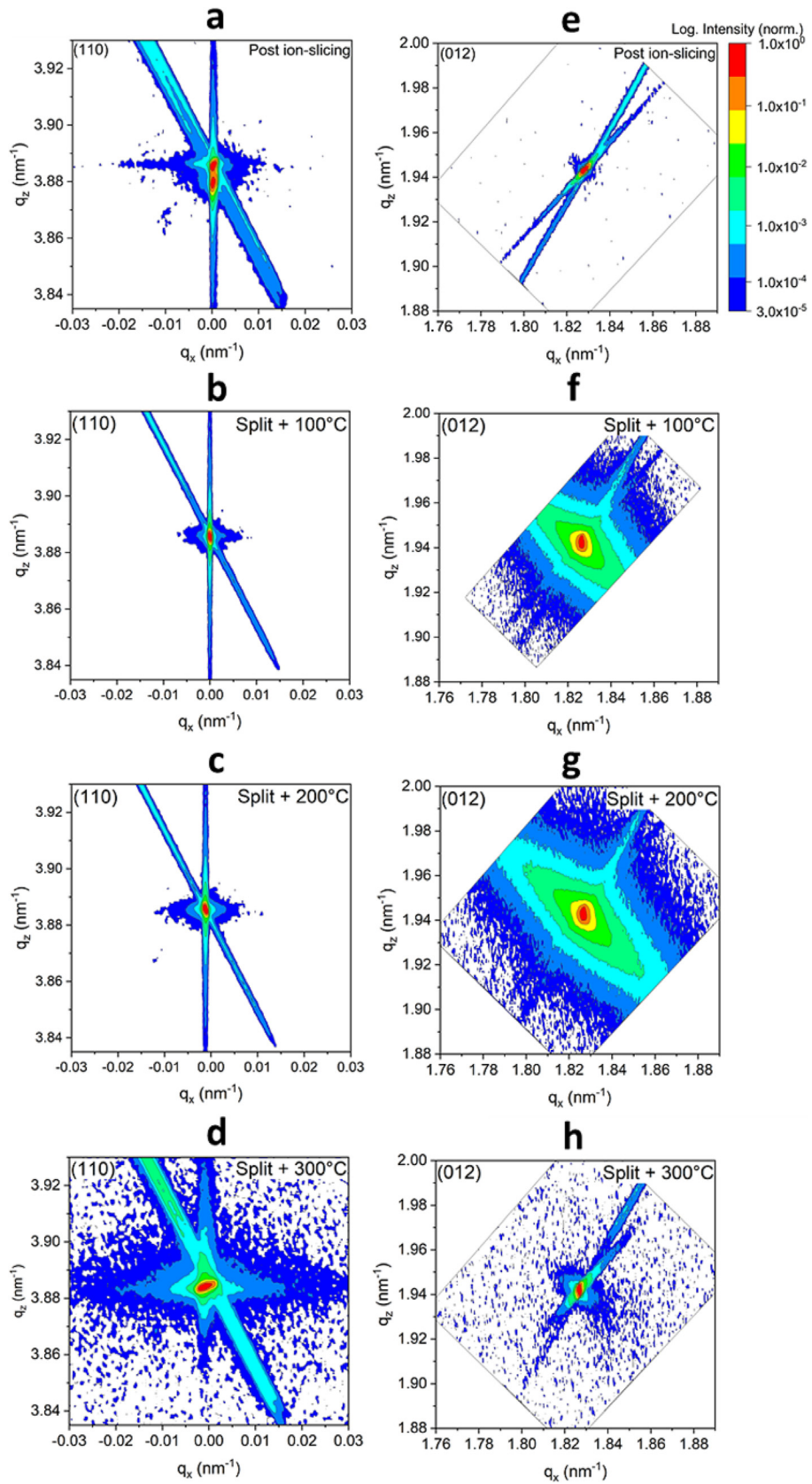


Fig. 2. Reciprocal space maps around the (110) and (012) LiNbO₃ lattice points. (a - d) RSMs of the (110) lattice point, from the as-split sample to the one annealed at 300 °C above the split temperature; (e - h) RSMs of the (012) lattice point, from the as-split sample to the one annealed at 300 °C above the split temperature;

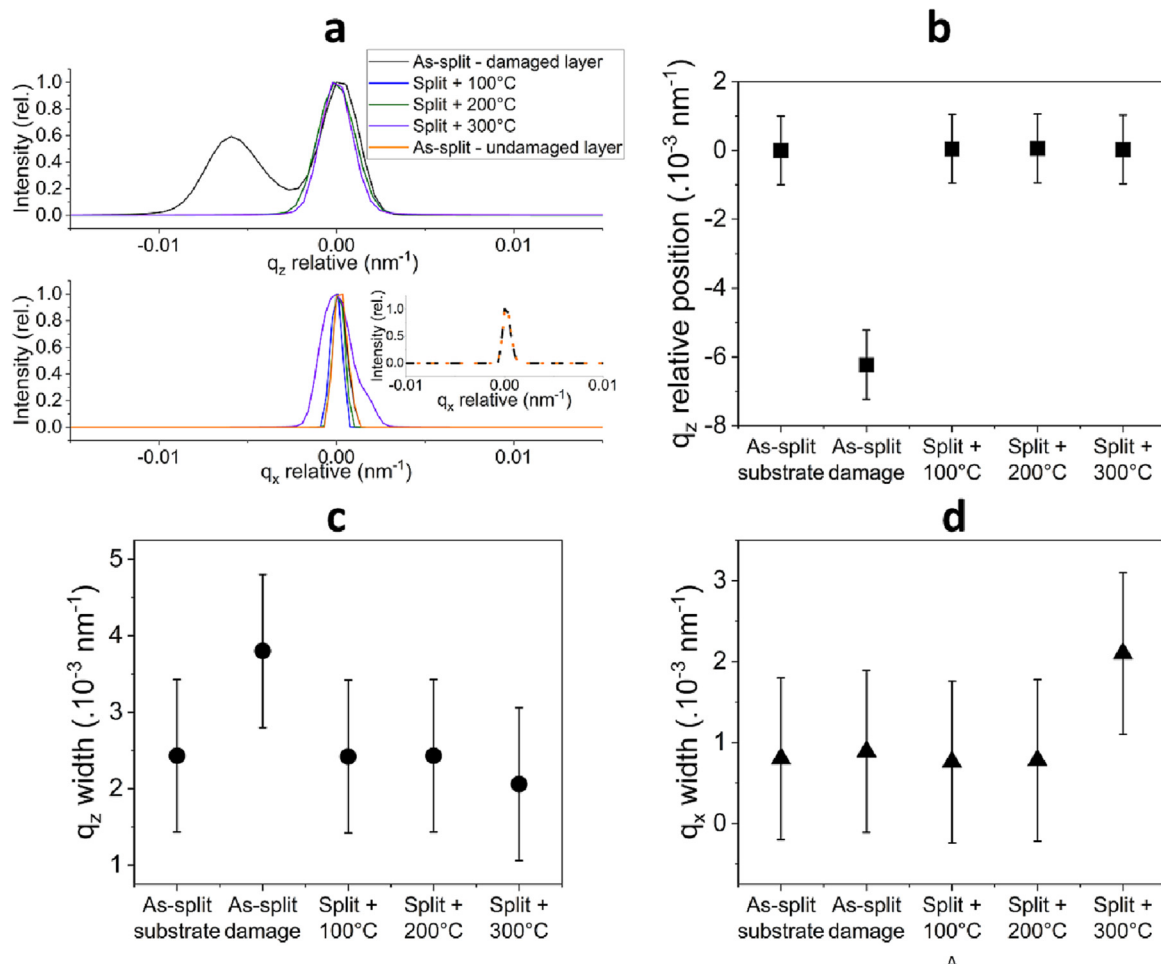


Fig. 3. Analysis of the mainly-coherent X-ray scattering of the LiNbO₃ (110) lattice point for post-CIS and annealed samples. (a) distribution profiles along the radial direction. q_z and q_x are in relative units ($q_z - q_{z,max}$) and ($q_x - q_{x,max}$). In the inset, the distribution of the coherent scattering along the angular direction related to the as-split damaged layer and the undamaged substrate; (b) relative position of the 110 reflection along q_z ; (c) width of the 110 reflection along q_z ; (d) width of the 110 peak along q_x .

affect the profiles. In Fig. 4(a), all the profiles show asymmetric features on the left side at $q_{z,relative} < 0$. Only the sample annealed up to 300 °C above the splitting temperature behaves differently and does not show asymmetric features. In Fig. 4(b), the tails of the distribution profiles of scattered intensities along q_x appear highly different from sample to sample, depending on the thermal history. The post-CIS sample shows a fast decay of the scattered intensities: for a module of the scattering vector equal to 0.01 nm⁻¹, normalized intensities are in the order of 10⁻⁴. Samples annealed at higher temperatures show a different DXS behavior: first, the scattered intensity decays much slower than in the previous samples, being still 1% of the maximum at $q_x = 0.01$ nm⁻¹. Both the Huang and Stokes-Wilson regions of the diffuse scattering are well distinguishable, and their crossover can be visually identified. The q_x values at the crossover are 0.016 nm⁻¹ and 0.028 nm⁻¹ for the crystals annealed at 100 °C and 200 °C above the splitting temperature, respectively. The crystal annealed at the highest temperature, i.e., 300 °C above the splitting temperature, shows a profile behavior characterized by a decay of the scattered intensity faster than the two previous cases, where crystals were annealed at a lower temperature. The Lorentzian tail decays faster than $I = qx^{-2}$, and both the Huang and Stokes-Wilson regions are not distinguishable, and the crossover is not found.

3.3. Damping of the Raman mode and stress calculation

The broadening of Raman modes, related to the degree of order and presence of lattice defects, have been used to estimate the process of recovery of the crystalline perfection of post-CIS LNO crystal after annealing. In particular, Fig. 5 (a) and 5(b) show the Raman spectra in the HV configuration and the zoom in the E(1TO) mode, from which the damping has been estimated. Fig. 5(c) shows the evolution of the damping of the E(1TO) Raman mode at 155 cm⁻¹ with the post-CIS annealing temperature, compared to the value from the unprocessed congruent black LNO crystal used as the reference. The damping proves larger in the LNO crystal as-split compared to the reference. Post CIS annealing produces the decreasing of the damping of the Raman mode, which recovers the reference LNO crystal value upon annealing at 200 °C above the split temperature. The highest annealing temperature, produces a slight further decreasing of the mode damping, while the statistic dispersion is deteriorated compared to the annealing at 200 °C above the split. The stress along the Z-direction (out-of-plane) and Y directions (in-plane) have been calculated from the shifts of wavenumbers of E(1TO) and E(6TO) Raman modes under the assumption of (i) no shear stress and (ii) $\sigma_x = \sigma_y$. The evolution of the residual stress, in Fig. 5(d), shows the crystals under compressive stress between -40 and -70 MPa along Y and X axis,

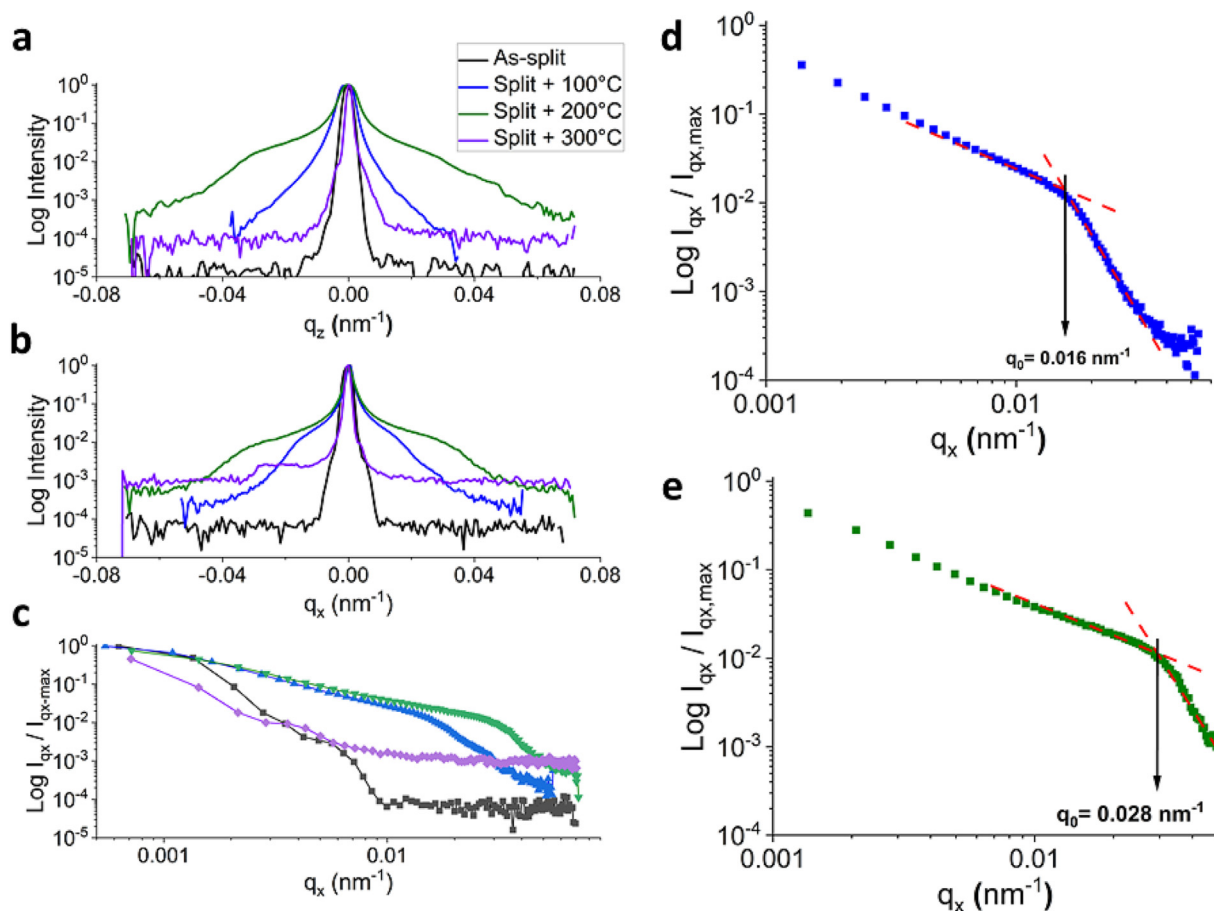


Fig. 4. Analysis of the diffuse X-ray scattering (DXS) of the LiNbO₃ (012) lattice point for post-CIS and annealed samples. q_z and q_x are in relative units ($q_z - q_{z,max}$) and ($q_x - q_{x,max}$). (a) Distribution of the scattered intensities profiles along q_z . (b) Distribution of the scattered intensities profiles along q_x . (c) Log-Log distribution of the scattered intensities along q_x relative facilitates the distinctions of the Huang and Stokes-Wilson regions of the diffuse scattering and the crossover between the two regions. (d) Log-Log distribution of the scattered intensities along q_x relative to the sample annealed at 100 °C above the split temperature. The two red lines represent behaviors of the diffuse scattering intensities in the Huang $I_H \approx q^{-2}$ and SW $I_{SW} \approx q^{-4}$ regions, respectively. The black arrow marks the crossover between the two regions at the value q_0 . (e) Log-Log distribution of the scattered intensities along q_x relative to the sample annealed at 200 °C above the split temperature. The two red lines represent behaviors of the diffuse scattering intensities in the Huang $I_H \approx q^{-2}$ and SW $I_{SW} \approx q^{-4}$ regions, respectively. The black arrow marks the crossover between the two regions at the value q_0 . (For interpretation of the references to color in this figure legend, the reader is referred to the web version of this article.)

while the stress along the Z-direction is slightly tensile and close to 0, in the range between + 8 and + 12 MPa. Annealing processes up to 200 °C above the split temperature result in minor changes in the stress status of the crystal. The annealing at 300 °C above the split increases the compressive stress in XY plane up to −277 MPa, while the stress along Z turns into slightly compressive.

3.4. TEM

Fig. 5(e–h) show bright-field and weak beam dark field TEM images of the crystals as-split and after annealing at 200 °C above the split temperature. The change in contrast is associated to the presence of lattice defects, allowing quantifying the extension of the damaged regions. The damaged region extends over a depth of 300 nm in as-split LNO crystals, as shown in Fig. 6(a) and (b). The lattice defects appear as large clusters of defects arranged in a spherical shape, which extend from the surface-near region to the end of the damaged region. Such clusters are clearly visible in both the dark- and bright-field TEM images. In the work from Lang and coworkers, such arrangement of defects appearing in He-implanted LNO upon low-temperature annealing are associated to dislocations loops [41]. After annealing at 200 °C above the split temperature, the depth of the damaged part of the LNO crystal is reduced to only 38 nm from the surface. Annealing at

higher temperatures does not show a clear difference in the TEM analysis. In the reference [41], the annealing at 500 °C resulted in the generation of so-called “heterogeneous strain” at the top surface of LNO [41]. This seems in good agreement with the TEM micrograph in Fig. 6(c) and (d).

4. Discussion

The comparison between Fig. 1(a) and 2(a) clearly shows the reason for starting from the post-CIS sample instead of the implanted one. The thermal and mechanical processes involved in the CIS produce extensive modifications of the crystalline damages introduced by the implantation. When interested in the physics of the recrystallization of post-CIS crystals, implanted samples cannot represent the microstructural damage. In particular, the “extended strain profile” has been replaced by only one peak additional to the expected for the undamaged crystal, and the Laue fringes are not visible anymore.

The second diffraction maximum in the reciprocal space around the (110) lattice point and the related diffraction peak at the smaller scattering vector module observed in the post-CIS sample indicates that the upper part of the crystal experiences a net tensile displacement. This is the residual CIS-induced damage mark: the d_{110} -spacing increases because of the lattice parameter expansion.

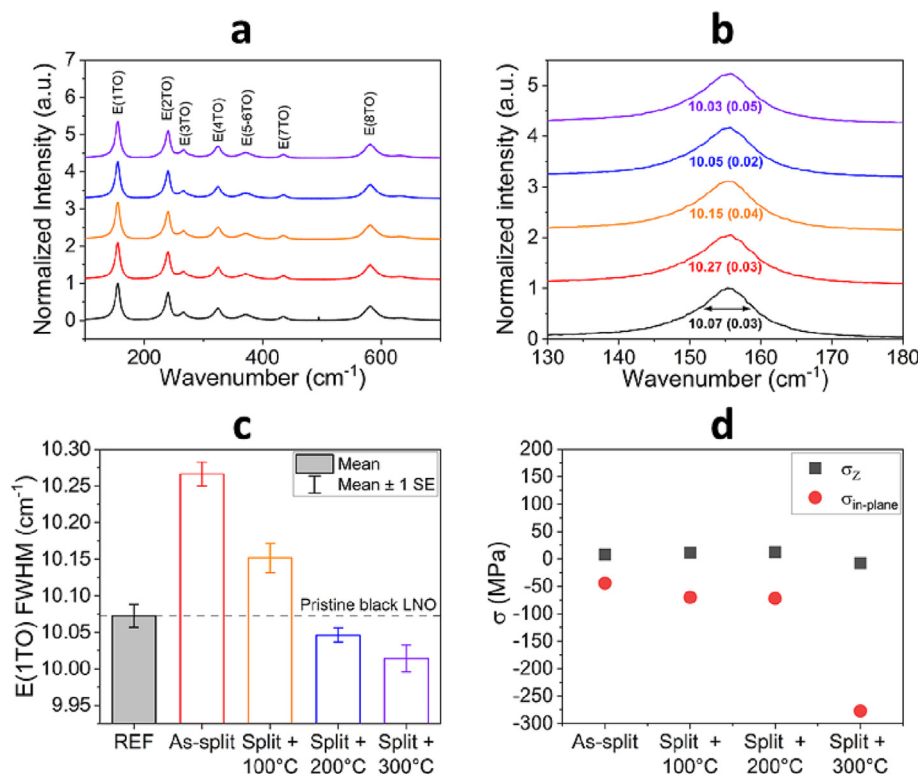


Fig. 5. (a) Micro-Raman spectroscopy spectra of the transversal modes of LNO crystal as-split and after annealing at the different temperatures collected in the HV configuration. (b) zoom into the E(1TO) mode for the crystals as-split and annealed at different temperatures. (c) Statistics of the damping of the Raman E(1TO) mode for crystal as-split and after annealing at different temperatures. Black filled box represents the reference bulk congruent LNO. Each sample have been measured in 20 points and 3 measurements at each point have been performed. The bar height is the mean value on the 20 measured points, the error bar are the standard error. (d) Stress measured along the directions out-of-plane (black) and in-plane (red) in crystals as-split and after annealing at different temperatures. (For interpretation of the references to color in this figure legend, the reader is referred to the web version of this article.)

The damaged part of the crystal presents a discontinuous strain status with respect to the undamaged substrate and a strain gradient, which causes the broadening of the distribution of the diffracted intensities in the radial direction. The annealing recovers the post-CIS crystal from the net tensile strain and reduces the dispersion of the coherent scattering along the radial direction of the (110) to the value for the undamaged LNO crystal, which remains constant at the different annealing temperatures. Except for the above-mentioned damaged-layer component in the post-CIS non-annealed sample, the 110 lattice point is found at the expected q_z position for all samples, which relates to the absence of a net strain affecting the crystal as the result of the thermal treatments. The analysis of the coherent scattering of the 110 lattice point along the azimuthal direction, i.e., q_x , provides additional information about the evolution of the crystallinity and the type of defects affecting it. In particular, the diffraction component related to the damaged layer in the untreated post-CIS is broadened in the radial direction, sensitive to the lattice strain, but as sharp as the reference in the angular direction, sensitive to the tilt of the atomic planes. This may indicate that point defects (vacancies, interstitials) or volume defects (clusters) homogeneously distributed represent the main source of lattice imperfections in post-CIS LNO crystals. Spherical point defects, or clusters of defects, generate a uniform displacement field that propagates around the core of the defect/cluster. However, this lattice displacement field, which intuitively modifies the atomic positions, has a minor influence on the tilt of the atomic planes.

Annealing the crystal at 300 °C upon the split temperature results in a minor sharpening of the scattered intensity distribution along the radial direction. However, we observe a major spread of

the scattered intensity along the azimuthal direction. In the ref. [41], the annealing at 750 °C of He-implanted LNO provoked the recrystallization of the most upper part of the crystal into a polycrystalline film. Accordingly, the formation of a polycrystalline layer increases the mosaicity and explains the broadening of the coherent scattering along the azimuthal direction showed by LNO upon annealing at 300 °C above the split temperature. The analysis of the diffuse scattering of the 012 reflections along q_z points out the presence of asymmetries in the DXS profiles, with features more pronounced at $q_{z-rel} < 0$, which relates to a predominance of vacancy-type defects [35,42]. The sample annealed 300 °C above the splitting temperature does not show such asymmetric features at $q_{z-rel} < 0$, highlighting the different nature of the revealed crystalline defects.

Information about the dimension of the defect clusters can be obtained from the profiles of the diffuse scattering along q_x [35,42]. The DXS profiles for the post-CIS and annealed LiNbO₃ crystals results in three different behaviors: (i) the untreated post-CIS sample shows diffuse scattering, mainly Gaussian and characterized by the rapid fall of the scattered intensities. The decay is much faster than the predictions from the theories of Huang and Stokes-Wilson, with the Lorentzian broadening constituted by a bump before the thermal diffuse scattering region. (ii) Samples annealed at 100 °C and 200 °C above the split temperature show DXS profiles characterized by a slow decay of the intensities that follows the predicted behavior in the Huang and Stokes-Wilson regions. (iii) The annealing at 300 °C above the split temperature produces a different pattern of DXS, with faster intensity decay compared to the lower annealing temperature.

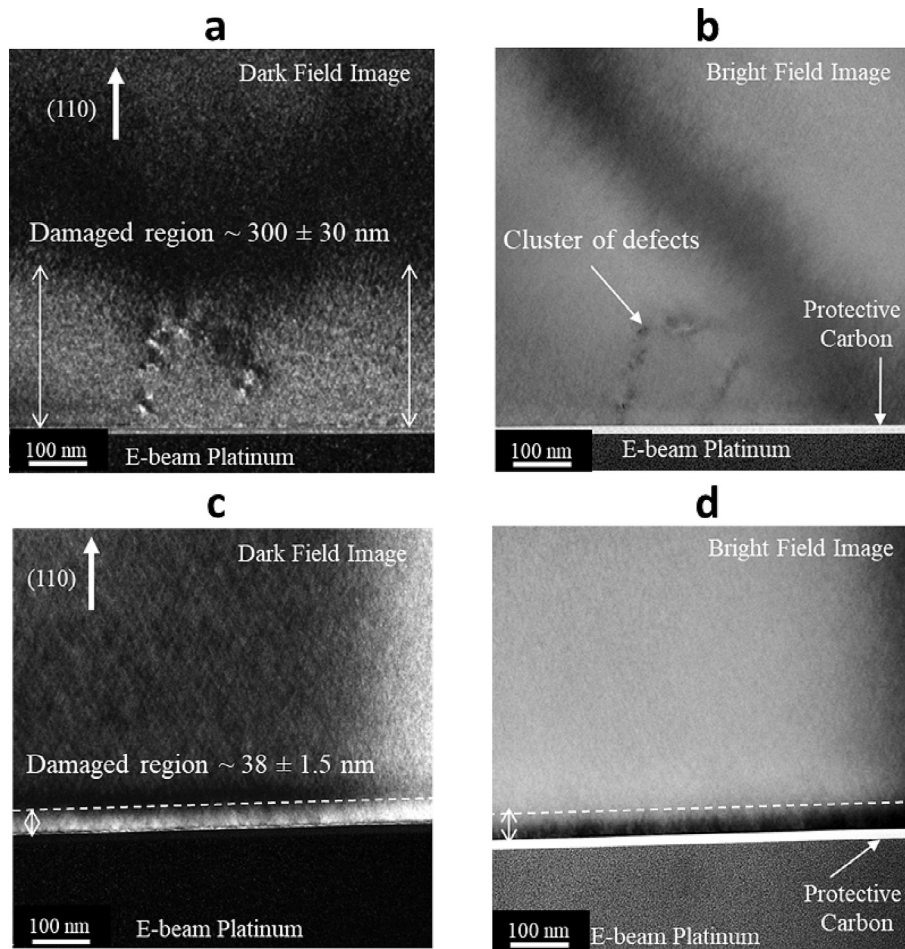


Fig. 6. TEM images of CIS-processed LNO crystals. (a) Weak-beam dark-field image using the 110 reflection at the [001] zone axis of the LNO crystal as-split. The change in color contrast highlights the damaged region, which is estimated to extend around 300 nm from the surface. (b) Bright-field TEM image of the LNO crystal as-split. The defects clusters appear as darker regions. (c) Weak-beam dark-field image using the 110 reflection at the [001] zone axis of the LNO crystal annealed at 200 °C above the split temperature. The change in color contrast highlights the damaged region, which is estimated to extend around 38 nm from the surface. (d) Bright-field TEM image of the LNO crystal as-split. The damaged region appears as a darker part close to the LNO surface.

According to the theories on diffuse X-ray scattering, when correlative enhancement between microstructural deviation from the ideality occurs, the tails of the Lorentzian profile become broader and their decay slower. When considering a cluster of defects, it generates a displacement field around the core. Observing the diffuse scattering in the region close to the Bragg peak, at a small q_x relative, means observing the far-field displacement, where $q \ll 1/R_0$ (R_0 is the radius of the defect core). This is the Huang region of the diffuse scattering. At larger q_x relative values, farther from the Bragg region, the near-field displacement is observed and the magnitude of the lattice displacements increases. The larger degree of disorder in this region – called Stokes-Wilson region – causes a faster decay of the scattered intensities. For even larger $q \gg 1/R_0$, the region of the defect core is approached where the lattice displacement increases again, provoking a decay of the scattered intensities with slope < -4 . However, this region is usually not observed due to the thermal scattering, which becomes predominant. In microstructural features like clusters of point defects or dislocation loops, the core of the defect will be represented by a part of the crystal affected by a certain strain field. In the case where many of these clusters with a narrow size distribution are included in the crystal, there will be a certain amount of the crystal lattice affected by the same strain field, which will scatter the radiation coherently. As expected, this raises the amplitude of the electric field and the scattered intensities. In the case of large defect clusters, the distance between the unstrained lattice (out from

the strain field of the defect or defects cluster) and the core of the defect will be large. That corresponds to seeing the effect of the correlation at small modules of the scattering vector along the angular direction q_x relative, i.e., in the vicinity of the lattice point representative of the unstrained lattice. When defects clusters are smaller, the distance between the unaffected lattice and the cluster's core will be smaller. Consequently, the coherent enhancement will be observed farther in the reciprocal space at larger modules of the scattering vector with respect to the lattice point. As always when treating correlative effects, the fundamental condition for observing a net variation in the Lorentzian profile decay is the existence of an “ordered pattern of disorder” in the structure, i.e., clusters with a narrow size distribution. Uncorrelated defects or systems presenting a broad distribution of defects size will not produce coherent enhancement. In this case, the scattered intensities decay fast until vanishing into the thermal diffuse scattering. Also, in the case of very large clusters, the diffuse scattering behaves differently from the description provided by Huang and Stokes-Wilson. In particular, the large size of defects reduces their concentration in the irradiated volume; since the intensity of the scattered radiation is proportional to the cluster concentration [35], only a minor, or even none, enhancement effect is observed. The Post-CIS sample does not show a remarkable enhancement of the diffuse scattering: this may be related to the large size and size distribution of defects clusters after the crystal ion-slicing. It seems reasonable that clusters reduce their size, and

perhaps the size distribution becomes narrower, promoting the coherent enhancement of the radiation scattered relatively far from the lattice point. After annealing, an average cluster size from around 60 nm down to around 35 nm is identified from the cross-over positions with increasing temperatures up to 100 °C and 200 °C above the split temperature, respectively.

Maeta and coworkers observed the behavior of the diffuse scattering in Ni single crystal implanted by Xe¹⁰⁺ ions [43]. In particular, the as-implanted crystal displayed diffuse scattering with typical Stokes-Wilson behavior, which disappears upon thermal annealing. The authors suggested a mechanism of rearrangement of the crystalline defects from point defects and their clusters, to dislocations loops and cascade [44]. Accordingly, post-CIS annealing produces an opposite effect in LNO crystals: point defects, clusters of point defects, and dislocations loops are predominant in the as-split crystal and they rearrange into smaller dislocations loops upon thermal annealing, raising the intensity of the diffuse scattering in the region farther from the Bragg peak (Stokes-Wilson). The rearrangement of point defects clusters into dislocation loops eventually acting as single dislocations, can explain the broadening of the 110 reflection rocking curve [26,45] in the crystal annealed at 300 °C above the split temperature. In this sample, the effect of the coherent enhancement of the scattered intensities vanishes as a consequence of the rearrangement of the clusters and loop into single dislocations, which translates into a mosaic-block microstructure in the region close to the surface. A similar effect has been recently reported in He-implanted LNO crystals upon annealing at high temperature [41]. Even though such a mosaic-block structure is more likely to occur in epitaxial thin films than in single-crystalline materials, the exceptional level of crystalline damage induced by the CIS process might eventually generate high mosaicity.

The rearrangement of the crystal associated with the decreasing the amount of damaged crystal has been confirmed by the TEM pictures in Fig. 6(a–d). In particular, the TEM image of the crystal as-split shows the damaged part extending up to a depth of 300 ± 30 nm, with spherical clusters related to dislocations loops [41]. Operating the annealing at 200 °C above the split temperature reduces the extension of the damaged layer to only 38 ± 1.5 nm beyond the LNO surface, as shown in Fig. 6(c) and (d); this result is in agreement with the calculation of the size of the defects clusters obtained by HRXRD, confirming the validity of our method. To compare results from DXS and TEM we assume that defects clusters are spherical and their diameter is approximately equal to the extension of the damaged layer. This hypothesis is enforced by the TEM image in Fig. 6(a), where the defect cluster diameter is approximately equal to the damaged zone of the crystal. Unfortunately, the resolution of the TEM analysis in Fig. 6(c) and (d) is insufficient to prove the presence of smaller clusters upon annealing at 200 °C above the split temperature.

Further increasing the annealing temperature does not promote an additional broadening of the diffuse scattering, at least along the (012) crystalline direction. Instead, crystallinity along the (110) out-of-plane direction appears degraded, with broadened distribution of the tilt of atomic planes.

The trend of improving the crystalline order with the annealing temperature is confirmed by Raman spectroscopy analyses. In particular, the damping of the E(1TO) mode, here used as a figure of merit of the lattice disorder, decreases upon annealing compared to the maximum value found in the crystal as-split. Annealing up to 200 °C above the split temperature results in the recovery of the damping compared to the black congruent LNO crystal used as a reference. The width of the Raman modes further decreases upon annealing at 300 °C above the split temperature, even if the decrease is accompanied by the broadening of the distribution, which relates to the fact that annealing at such high temperature

influences the crystal in aspects related not only to the CIS-induced damage. The discrepancies between the diffraction and spectroscopic methods are related to the sample annealed at the highest temperature, whose microstructure seems already substantially recovered from Raman spectroscopy, while the HRXRD analysis points out the degradation of the crystallinity. The differences in the probed volumes between HRXRD and Raman and a different sensitivity for different types of lattice disorder must be considered for evaluating results from the different techniques. Raman spectroscopy uses a green laser that penetrates the LNO crystal around 1 µm in depth, while X-rays penetration extend over a range of several microns. With the CIS-induced defects being located at the top of the crystal and extending around 300 nm in-depth before the annealing, Raman spectroscopy is probably more sensitive to the effects induced by such defects. Raman spectroscopy being much more sensitive to the surface maintains the sensitivity to the crystalline damage even if the thickness of the damaged layer decreases. Also, HRXRD, especially when the coherent scattering is taken into account, sees the effect of the crystalline imperfection – such as strain gradients and tilt – more than the crystalline imperfection itself. Lattice defects might be invisible in XRD patterns if they do not produce any of the observables. Instead, Raman is also sensitive to the defect itself because of its influence on the vibrational state of the crystal. Accordingly, a second hypothesis is that the annealing at relatively low temperature already recovers the crystal from the net tensile strain observed in the CIS-damaged part and revealed by HRXRD, but a high density of lattice defects remains in the crystal and is detected by Raman. The degradation of the crystallinity observed by HRXRD after annealing at 300 °C above the split temperature can be related to the phenomena of deterioration of LNO, occurring simultaneously with the recovery of the residual CIS-induced damages. The effect of the latter is predominant in Raman spectroscopy due to its higher surface-sensitivity, which results in a further decrease of the damping of the Raman mode, while the degradation of the bulk is visible in terms of deterioration of the statistic dispersion of the Raman measurements. According to theoretical calculations, the E(1TO) mode at 155 cm^{-1} is linked to Nb-O octahedron distortions due to Nb-O bonds stretching, Li-O octahedron distortion due to Li-O bonds stretching, and two sets of O-Nb-O and O-Li-O bonds bending [46]. The increasing dispersion of the damping of this mode might be related to the creation of oxygen vacancies due to O diffusion and LiO₂ evaporation upon LNO congruent crystal partial decomposition.

Raman spectroscopy being much less sensitive to the bulk, the degradation of the LNO crystallinity due to the high annealing temperature results minor compared to the effect of the recovery of the CIS-induced damage. The broadening of the Bragg peak along the in-plane (q_x component of the scattering vector) direction may be also related to the generation of residual stress, which was confirmed by the higher value of compressive stress extracted from the Raman measurements.

5. Conclusions

This work evaluates the influence of thermal annealing on the crystalline quality and level of stress in X-cut LiNbO₃ single crystals undergoing crystal ion-slicing fabrication processes. The approach based on the study of the X-ray diffuse scattering, complemented by Raman spectroscopy and TEM allowed the following findings:

- The CIS process leaves a part of the crystal under a tensile strain in the out-of-plane direction; the lattice swelling is typically observed in ion-implanted crystals as an effect of the in-plane compressive stress generated.

- The crystal recovered from the net tensile strain induced by the CIS upon annealing at 100 °C above the splitting temperature; further increases of the annealing temperature have minor effects on the coherent scattering features.
- The thermal annealing promotes the recovery of the crystalline perfection through the rearrangement of clusters of point defects into dislocations loops. TEM analyses point out the reduction of the extension of the damaged layer up to 38 nm upon annealing at 200 °C above the split temperature. This result is in agreement with the value calculated from the diffuse scattering, i.e., 35 nm, under the assumption that defects clusters are spherical and their diameter is approximately equal to the extension of the damaged layer.
- Thermal annealing at 300 °C above the splitting produces a fast decay of the diffuse scattering, which hide the correlative related to the recovery of the residual CIS-induced damage, now affecting the very near-surface region. The broadening of the Bragg peaks in the in-plane direction may be related to the increasing of the dislocations density resulting from the dislocation loops rearrangement and the level of compressive stress calculated by Raman spectroscopy.

In conclusion, HRXRD and DXS studies, complemented by Raman spectroscopy and TEM analyses, point out that the recovery from the CIS-induced crystalline damage in LNO (and likely in every crystalline material) occurs through recrystallization of clusters of point defects into dislocation loops and eventually non-correlated dislocations.

6. Data availability statement

The raw/processed data required to reproduce these findings cannot be shared at this time as the data also forms part of an ongoing study.

CRediT authorship contribution statement

Simone Dolabella: Validation, Formal analysis, Investigation, Writing – review & editing. **Alexandre Reinhardt:** Resources, Writing – review & editing. **Ausrine Bartasyte:** Methodology, Validation, Investigation, Writing – review & editing. **Samuel Margueron:** Methodology, Validation, Investigation, Writing – review & editing. **Amit Sharma:** Formal analysis, Investigation, Writing – review & editing. **Xavier Maeder:** Writing – review & editing. **Alex Dommann:** Formal analysis, Writing – review & editing. **Antonia Neels:** Formal analysis, Resources, Writing – review & editing. **Aurelio Borzi:** Conceptualization, Methodology, Validation, Formal analysis, Investigation, Writing – original draft, Supervision.

Data availability

Data will be made available on request.

Declaration of Competing Interest

The authors declare the following financial interests/personal relationships which may be considered as potential competing interests: Alexandre Reinhardt reports a relationship with French Alternative Energies and Atomic Energy Commission Electronics and Information Technology Laboratory that includes: employment.

References

- [1] P.D. Townsend, Optical effects of ion implantation, Rep. Prog. Phys. 50 (1987) 501–558, <https://doi.org/10.1088/0034-4885/50/5/001>.
- [2] G.D.H. King, M.C. Bone, B.L. Weiss, D.W. Weeks, Ion implanted optical waveguides in LiNbO₃, Electron. Lett. 17 (1981) 897, <https://doi.org/10.1049/el:19810625>.
- [3] S.A.M. Al-Chalabi, B.L. Weiss, K.P. Homewood, Optical properties of rapid furnace annealed He⁺ implanted LiNbO₃ waveguides, Nucl. Instrum. Methods Phys. Res. Sect. B Beam Interact. Mater. At. 28 (1987) 255–258, [https://doi.org/10.1016/0168-583X\(87\)90114-5](https://doi.org/10.1016/0168-583X(87)90114-5).
- [4] G.L. Destefanis, J.P. Gailliard, E.L. Ligeon, S. Valette, B.W. Farmery, P.D. Townsend, A. Perez, The formation of waveguides and modulators in LiNbO₃ by ion implantation, J. Appl. Phys. 50 (1979) 7898–7905, <https://doi.org/10.1063/1.325982>.
- [5] V.V. Atuchin, Causes of refractive indices changes in He-implanted LiNbO₃ and LiTaO₃ waveguides, Nucl. Instrum. Methods Phys. Res. Sect. B Beam Interact. Mater. At. 168 (2000) 498–502, [https://doi.org/10.1016/S0168-583X\(00\)00038-0](https://doi.org/10.1016/S0168-583X(00)00038-0).
- [6] M. Gorisse, R. Bauder, H.-J. Timme, H.-P. Friedrich, L. Dours, P. Perreau, A. Ravix, R. Lefebvre, G. Castellan, C. Maeder-Pachurka, M. Bousquet, A. Reinhardt, High Frequency LiNbO₃ Bulk Wave Resonator, in: 2019 Jt. Conf. IEEE Int. Freq. Control Symp. Eur. Freq. Time Forum EFTF/IEEE, IEEE, Orlando, FL, USA, 2019: pp. 1–2, <https://doi.org/10.1109/FCS.2019.8856017>.
- [7] M. Pijolat, S. Loubriat, S. Queste, D. Mercier, A. Reinhardt, E. Defay, C. Deguet, L. Clavelier, H. Moriceau, M. Aid, S. Ballandras, Large electromechanical coupling factor film bulk acoustic resonator with X-cut LiNbO₃ layer transfer, Appl. Phys. Lett. 95 (18) (2009) 182106.
- [8] F.V. Pop, A.S. Kochhar, G. Vidal-Alvarez, G. Piazza, Investigation of Electromechanical Coupling and Quality Factor of X-Cut Lithium Niobate Laterally Vibrating Resonators Operating Around 400 MHz, J. Microelectromech. Syst. 27 (2018) 407–413, <https://doi.org/10.1109/JMEMS.2018.2817842>.
- [9] A. Bartasyte, S. Margueron, T. Baron, S. Oliveri, P. Boulet, Toward high-quality epitaxial LiNbO₃ and LiTaO₃ thin films for acoustic and optical applications, Adv. Mater. Interfaces 4 (8) (2017) 1600998.
- [10] M. Levy, R.M. Osgood, R. Liu, L.E. Cross, G.S. Cargill, A. Kumar, H. Bakhru, Fabrication of single-crystal lithium niobate films by crystal ion slicing, Appl. Phys. Lett. 73 (16) (1998) 2293–2295.
- [11] H. Han, L. Cai, H. Hu, Optical and structural properties of single-crystal lithium niobate thin film, Opt. Mater. 42 (2015) 47–51, <https://doi.org/10.1016/j.optmat.2014.12.016>.
- [12] S. Sumie, H. Takamatsu, T. Morimoto, Y. Nishimoto, Y. Kawata, T. Horiuchi, H. Nakayama, T. Kita, T. Nishino, Analysis of lattice defects induced by ion implantation with photo-acoustic displacement measurements, J. Appl. Phys. 76 (1994) 5681–5689, <https://doi.org/10.1063/1.357074>.
- [13] L.W. Hobbs, Application of transmission electron microscopy to radiation damage in ceramics, J. Am. Ceram. Soc. 62 (1979) 267–278, <https://doi.org/10.1111/j.1151-2916.1979.tb09480.x>.
- [14] E. Zolotoyabko, Y. Avrahami, W. Sauer, T.H. Metzger, J. Peisl, Strain profiles in He-implanted waveguide layers of LiNbO₃ crystals, Mater. Lett. 27 (1996) 17–20, [https://doi.org/10.1016/0167-577X\(95\)00256-1](https://doi.org/10.1016/0167-577X(95)00256-1).
- [15] Y. Avrahami, E. Zolotoyabko, Structural modifications in He-implanted waveguide layers of LiNbO₃, Nucl. Instrum. Methods Phys. Res. Sect. B Beam Interact. Mater. At. 120 (1996) 84–87, [https://doi.org/10.1016/S0168-583X\(96\)00484-3](https://doi.org/10.1016/S0168-583X(96)00484-3).
- [16] A.M. Radojevic, M. Levy, H. Kwak, R.M. Osgood, Strong nonlinear optical response in epitaxial liftoff single-crystal LiNbO₃ films, Appl. Phys. Lett. 75 (19) (1999) 2888–2890.
- [17] B.-X. Xiang, J. Guan, Y. Jiao, L. Wang, Fabrication of ion-sliced lithium niobate slabs using helium ion implantation and Cu-Sn bonding: Fabrication of ion-sliced lithium niobate slabs, Phys. Status Solidi A 211 (2014) 2416–2420, <https://doi.org/10.1002/pssa.201431138>.
- [18] X. Bai, Y. Shuai, C. Gong, C. Wu, W. Luo, R. Böttger, S. Zhou, W. Zhang, Surface modifications of crystal-ion-sliced LiNbO₃ thin films by low energy ion irradiations, Appl. Surf. Sci. 434 (2018) 669–673, <https://doi.org/10.1016/j.apsusc.2017.10.184>.
- [19] Y. Shuai, C. Gong, X. Bai, C. Wu, W. Luo, R. Böttger, S. Zhou, B. Tian, W. Zhang, Fabrication of Y128- and Y36-cut lithium niobate single-crystalline thin films by crystal-ion-slicing technique, Jpn. J. Appl. Phys. 57 (2018) 04FK05, <https://doi.org/10.7567/JJAP.57.04FK05>.
- [20] A.Y. Lushkin, V.B. Nazarenko, K.N. Pilipchak, V.F. Shnyukov, A.G. Naumovets, The impact of annealing and evaporation of crystals on their surface composition, J. Phys. Appl. Phys. 32 (1999) 9–15, <https://doi.org/10.1088/0022-3727/32/1/003>.
- [21] M. Birkholz, Thin Film Analysis by X-Ray Scattering, 1st ed., Wiley, 2005, <https://doi.org/10.1002/3527607595>.
- [22] J.I. Langford, A.J.C. Wilson, Scherrer after sixty years: a survey and some new results in the determination of crystallite size, J. Appl. Crystallogr. 11 (1978) 102–113, <https://doi.org/10.1107/S0021889878012844>.
- [23] A. Monshi, M.R. Foroughi, M.R. Monshi, Modified scherrer equation to estimate more accurately nano-crystallite size using XRD, World J. Nano Sci. Eng. 02 (2012) 154–160, <https://doi.org/10.4236/wjnse.2012.23020>.
- [24] A. Borzi, S. Dolabella, W. Szymt, J. Geler-Kremer, S. Abel, J. Fompeyrine, P. Hoffmann, A. Neels, Microstructure analysis of epitaxial BaTiO₃ thin films on SrTiO₃-buffered Si: Strain and dislocation density quantification using HRXRD methods, Materialia 14 (2020) 100953, <https://doi.org/10.1016/j.mtl.2020.100953>.
- [25] H.-M. Wang, J.-P. Zhang, C.-Q. Chen, Q. Fareed, J.-W. Yang, M.A. Khan, AlN/AlGaIn superlattices as dislocation filter for low-threading-dislocation thick

- AlGaIn layers on sapphire, *Appl. Phys. Lett.* 81 (2002) 604–606, <https://doi.org/10.1063/1.1494858>.
- [26] T. Metzger, R. Höppler, E. Born, O. Ambacher, M. Stutzmann, R. Stömmer, M. Schuster, H. Göbel, S. Christiansen, M. Albrecht, H.P. Strunk, Defect structure of epitaxial GaN films determined by transmission electron microscopy and triple-axis X-ray diffractometry, *Philos. Mag. A* 77 (1998) 1013–1025, <https://doi.org/10.1080/01418619808221225>.
- [27] A. Sharma, S. Mohan, S. Suwas, New insights into microstructural evolution of epitaxial Ni–Mn–Ga films on MgO (1 0 0) substrate by high-resolution X-ray diffraction and orientation imaging investigations, *Philos. Mag.* 98 (2018) 819–847, <https://doi.org/10.1080/14786435.2017.1418094>.
- [28] S. Dolabella, A. Borzi, A. Dommann, A. Neels, Lattice strain and defects analysis in nanostructured semiconductor materials and devices by high-resolution X-ray diffraction: theoretical and practical aspects, *Small Methods* 6 (2) (2022) 2100932.
- [29] V.S. Kopp, V.M. Kaganer, B. Jenichen, O. Brandt, Analysis of reciprocal space maps of GaN(0001) films grown by molecular beam epitaxy, *J. Appl. Crystallogr.* 47 (2014) 256–263, <https://doi.org/10.1107/S1600576713032639>.
- [30] A. Benediktovitch, A. Zhylik, T. Ulyanenkova, M. Myronov, A. Ulyanenkova, Characterization of dislocations in germanium layers grown on (011)- and (111)-oriented silicon by coplanar and noncoplanar X-ray diffraction, *J. Appl. Crystallogr.* 48 (2015) 655–665, <https://doi.org/10.1107/S1600576715005397>.
- [31] V. Lashkaryov Institute of Semiconductor Physics, NAS of Ukraine, 41, prospect Nauky, 03028 Kyiv, Ukraine, N.V. Safriuk, X-ray diffraction investigation of GaN layers on Si(111) and Al₂O₃ (0001) substrates, *Semicond. Phys. Quantum Electron. Optoelectron.* 16 (2013) 265–272, <https://doi.org/10.15407/spqe016.03.265>.
- [32] P.F. Fewster, Multicrystal X-ray diffraction of heteroepitaxial structures, *Appl. Surf. Sci.* 50 (1991) 9–18, [https://doi.org/10.1016/0169-4332\(91\)90133-5](https://doi.org/10.1016/0169-4332(91)90133-5).
- [33] P.F. Fewster, Advances in the structural characterisation of semiconductor crystals by X-ray scattering methods, *Prog. Cryst. Growth Charact. Mater.* 48–49 (2004) 245–273, <https://doi.org/10.1016/j.pcrysgrow.2005.03.001>.
- [34] A. Borzi, R. Zboray, S. Dolabella, S. Brun, F. Telmont, P. Kupferschmied, J.-F.-L. Néel, P. Drljaca, G. Fiorucci, A. Dommann, A. Neels, HRXRD and micro-CT multiscale investigation of stress and defects induced by a novel packaging design for MEMS sensors, *Appl. Mater. Today* 29 (2022) 101555, <https://doi.org/10.1016/j.apmt.2022.101555>.
- [35] P.H. Dederichs, Diffuse scattering from defect clusters near bragg reflections, *Phys. Rev. B* 4 (1971) 1041–1050, <https://doi.org/10.1103/PhysRevB.4.1041>.
- [36] H.-C. Huang, J.I. Dadap, I.P. Herman, H. Bakhru, R.M. Osgood, Micro-Raman spectroscopic visualization of lattice vibrations and strain in He⁺- implanted single-crystal LiNbO₃, *Opt. Mater. Express* 4 (2014) 338, <https://doi.org/10.1364/OME.4.000338>.
- [37] H.E. Swanson, Standard x-ray diffraction powder patterns, (n.d.).
- [38] J.-S. Moulet, M. Pijolat, J. Dechamp, F. Mazen, A. Tauzin, F. Rieutord, A. Reinhardt, E. Defay, C. Deguet, B. Ghyselen, L. Clavelier, M. Aid, S. Ballandras, C. Mazure, High piezoelectric properties in LiNbO₃ transferred layer by the Smart Cut[®] x2122; technology for ultra wide band BAW filter applications, in: 2008 IEEE Int. Electron Devices Meet., IEEE, San Francisco, CA, USA, 2008: pp. 1–4, <https://doi.org/10.1109/IEDM.2008.4796785>.
- [39] S. Margueron, A. Bartasyte, A.M. Glazer, E. Simon, J. Hlinka, I. Gregora, J. Gleize, Resolved E-symmetry zone-centre phonons in LiTaO₃ and LiNbO₃, *J. Appl. Phys.* 111 (10) (2012) 104105.
- [40] A. Bartasyte, V. Plausinaitiene, A. Abrutis, T. Murauskas, P. Boulet, S. Margueron, J. Gleize, S. Robert, V. Kubilius, Z. Saltyte, Residual stresses and clamped thermal expansion in LiNbO₃ and LiTaO₃ thin films, *Appl. Phys. Lett.* 101 (12) (2012) 122902, <https://doi.org/10.1063/1.4752448>.
- [41] E. Lang, T. Beechem, A. McDonald, T. Friedmann, R.H. Olsson, J.O. Stevens, B.G. Clark, K. Hattar, Defect structures as a function of ion irradiation and annealing in LiNbO₃, *Thin Solid Films* 768 (2023) 139719.
- [42] M. Moreno, B. Jenichen, V. Kaganer, W. Braun, A. Trampert, L. Däweritz, K.H. Ploog, MnAs nanoclusters embedded in GaAs studied by x-ray diffuse and coherent scattering, *Phys. Rev. B* 67 (2003) 235206, <https://doi.org/10.1103/PhysRevB.67.235206>.
- [43] H. Maeta, N. Matsumoto, T. Kato, H. Sugai, H. Ohtsuka, M. Sataka, Structure of defect cascades in heavy ions-irradiated nickel by X-ray diffuse scattering, *Nucl. Instrum. Methods Phys. Res. Sect. B Beam Interact. Mater. At.* 242 (1–2) (2006) 546–549.
- [44] P. Ehrhart, Investigation of radiation damage by X-ray diffraction, *J. Nucl. Mater.* 216 (1994) 170–198, [https://doi.org/10.1016/0022-3115\(94\)90012-4](https://doi.org/10.1016/0022-3115(94)90012-4).
- [45] R. Chierchia, T. Böttcher, H. Heinke, S. Einfeldt, S. Figge, D. Hommel, Microstructure of heteroepitaxial GaN revealed by x-ray diffraction, *J. Appl. Phys.* 93 (2003) 8918–8925, <https://doi.org/10.1063/1.1571217>.
- [46] Y. Repelin, E. Husson, F. Bennani, C. Proust, Raman spectroscopy of lithium niobate and lithium tantalate. Force field calculations, *J. Phys. Chem. Solids* 60 (1999) 819–825, [https://doi.org/10.1016/S0022-3697\(98\)00333-3](https://doi.org/10.1016/S0022-3697(98)00333-3).